KURUSHINA, V., PRATHURU, A., SOMAN, A., HOSSAIN, M., CAI, Q., HORRI, B.A. and FAISAL, N.H. 2025. Cohesive zone model for the thermomechanical deformation of a high temperature tubular solid oxide electrolysis cell. *Engineering fracture mechanics* [online], 318, article number 110987. Available from: https://doi.org/10.1016/j.engfracmech.2025.110987

Cohesive zone model for the thermomechanical deformation of a high temperature tubular solid oxide electrolysis cell.

KURUSHINA, V., PRATHURU, A., SOMAN, A., HOSSAIN, M., CAI, Q., HORRI, B.A. and FAISAL, N.H.

2025

Engineering Fracture Mechanics 318 (2025) 110987

Contents lists available at ScienceDirect

Engineering Fracture Mechanics

journal homepage: www.elsevier.com/locate/engfracmech

Cohesive zone model for the thermomechanical deformation of a high temperature tubular solid oxide electrolysis cell

Victoria Kurushina [a,c,*], Anil Prathuru [a,*], Ajith Soman [b], Mamdud Hossain [a], Qiong Cai [b], Bahman Amini Horri [b], Nadimul Haque Faisal [a,*]

[a] School of Computing, Engineering and Technology, Robert Gordon University, Aberdeen AB10 7GJ, UK
[b] Department of Chemical & Process Engineering, University of Surrey, Guildford GU2 7XH, UK
[c] Industrial University of Tyumen, Tyumen 625 000, Russia

A R T I C L E I N F O

Keywords:
Solid oxide electrolysis cell
Debonding
Crack growth
Cohesive zone model
Fracture analysis
Thermomechanical deformation

A B S T R A C T

High-temperature processes for hydrogen production unlock the potential for high energy efficiency combined with a relatively low environmental impact. However, structural integrity should be carefully considered. Solid oxide electrolysis cells (SOEC) employ a range of ceramic and metallic materials capable of withstanding high temperatures, ranging from 500 °C to 1000 °C, while facilitating active electrochemical reactions. The present structural analysis focuses on the challenge of anticipating the formation of debonding cracks at the interfaces of layers (assumed non-porous) within a single SOEC cell with a tubular design and a metal support. This study includes implementation of material properties for ceramic mixtures, model verification, analysis of deformation, stresses, crack formation using the cohesive zone model (CZM) – a method commonly used to simulate the process of crack initiation and propagation. In this pioneering research, several potential areas of debonding have been identified, with the primary concentration occurring around the fixed-end boundaries. Findings reveal a temperature-dependent curvature for the maximum expected total deformations, where a linear growth pattern turns into a random pattern, peaking at 750 °C. Up to eight deformation zones, which could potentially serve as crack initiation locations, are identified near the fixed boundaries, and up to four zones are indicated by deformation contours for the main body of the tubular cell model. The study establishes and reports the evolution of these debonding zones through the high-temperature operating range.

1. Introduction

Solid oxide electrolyser technology is vital for advancing sustainable energy production due to its outstanding efficiency in converting heat and electrical energy into hydrogen or syngas [1–3]. This high-temperature technology enables the utilisation of residual heat and naturally abundant feedstock materials, such as water and carbon dioxide. The use of such sustainable materials reduces the pressure on the environment to produce energy carriers. Solid oxide electrolysis cells (SOEC) (Fig. 1) are on the verge of transitioning to large-scale hydrogen production for needs of hydrogen-powered vehicles, integrated renewable energy systems, and grid-scale

* Corresponding authors at: School of Computing, Engineering and Technology, Robert Gordon University, Aberdeen AB10 7GJ, UK (V. Kurushina).

E-mail addresses: v.kurushina@outlook.com (V. Kurushina), a.prathuru@rgu.ac.uk (A. Prathuru), n.h.faisal@rgu.ac.uk (N.H. Faisal).

https://doi.org/10.1016/j.engfracmech.2025.110987
Received 9 November 2024; Received in revised form 5 February 2025; Accepted 25 February 2025
Available online 27 February 2025

Nomenclature

Abbreviations

Ag	Silver
Al	Aluminium
CZM	Cohesive Zone Model
GDC	Gadolinium-Doped Ceria
LSCF	Lanthanum Strontium Cobalt Ferrite
NiO	Nickel Oxide
SOEC	Solid Oxide Electrolysis Cell
Ti	Titanium
V	Vanadium
YSZ	Yttria-Stabilised Zirconia

Greek symbols

α	Artificial damping coefficient
β	Non-dimensional parameter of scaling (weighting) of the tangential component of displacement
δ	Displacement jump
δ_n	Normal component of displacement jump
δ_t	Tangential component of displacement jump
δ_n^c	Normal displacement jump at the completion of debonding
δ_t^c	Tangential displacement jump at the completion of debonding
δ_n^*	Normal displacement jump at the maximum normal cohesive traction
δ_t^*	Tangential displacement jump at maximum tangential cohesive traction
ε	Strain vector
η	Coefficient characterizing displacement jumps
λ	Non-dimensional effective displacement jump
λ_{cr}	Value of λ at which the maximum effective traction occurs
λ_i	Estimate of the Lagrangian multiplier
λ^{max}	Maximum of the λ history
σ	Stress vector
ϕ_i	Contact gap or penetration between the surfaces

Latin symbols

B	Matrix of shape functions for each element of the model
D	Elasticity matrix
D_n	Damage parameter
d_m	Coefficient characterizing displacement jumps
f	Arbitrary function
f_a	Applied force
f_{ext}	External forces
f_{int}	Internal forces
I	Index of equality constraint
K	Stiffness matrix
K_n	Normal cohesive stiffness
K_t	Tangential cohesive stiffness
K	Penalty parameter
L	Original Lagrangian of the system
L_{aug}	Augmented Lagrangian of the system
m	Iteration number
n	Normal direction
t	Tangential direction
T_n	Normal cohesive traction
T_t	Tangential cohesive traction
T_n^{max}	Maximum normal cohesive traction
T_t^{max}	Maximum tangential cohesive traction
u	Nodal displacement vector
u^{top}	Displacement of the top adjacent surface
u^{bottom}	Displacement of the bottom adjacent surface
V	Volume
x	Arbitrary variable

energy storage [4]. For this purpose, novel SOEC designs are in demand, necessitating simulations and innovations at the microscale, cell- and stack-levels, including structural, fluid dynamics and Multiphysics type of analyses [1].

Fracture mechanics is a critical component in the analysis of structural stability, to ensure the long-term reliability of solid oxide electrolysers. High-temperature SOECs are structurally subjected to temperatures ranging from 500 °C to 1000 °C, where they become susceptible to fracture-related degradation, and understanding and predicting the initiation and propagation of cracks becomes essential. Brittle, ductile, fatigue, creep, corrosion, and debonding fractures are commonly discussed in the literature [5–9], and debonding fractures are most relevant to SOECs due to frequent fracturing at interfaces, compromising the electrical characteristics. Similar problems with electrochemistry affected by debonding arise in the all-solid-state batteries [10].

Debonding stands for a primary way of interfacial failure, where the separation of two bonded surfaces takes place. This phenomenon is common in composite materials, layered structures, adhesive joints and coatings, where surfaces are held together by adhesive and cohesive forces. Debonding manifests when these forces are overcome by external stresses. Debonding is rare in homogeneous, bulk materials and is considered separately from fractures in this setting. Fracturing modes describing the mechanism behind the propagation generally include Mode I (opening mode), Mode II (sliding mode), Mode III (tearing mode), and Mixed-Mode fractures. Debonding, among the fractures, can be characterized with the Mode I mechanism, where tensile stress is perpendicular to the crack surface, Mode II mechanism, where the crack surfaces slide over one another, and Mixed-Mode mechanism, where debonding is driven by both tensile and shear stresses and the interfacial fracture grows in both directions.

Debonding in relevant structures has been studied at various scales, including at a molecular level using molecular dynamics [11,12] and at a mesoscale with the finite element approach [13–15], and also with a combination of approaches in a multiscale way [16,17]. The literature considered various structures subjected to debonding failure: bimaterial sample near a V-notch [18], concrete-filled steel tubes [19], strengthened beams [20,21], composite beams [22,23], T-stiffened composite plates [24], thin brittle layer deposited on a substrate [25], laminated structural battery [26], polymer composites [27], reinforced concrete block [28,29], and many others. Already undertaken research considered the development of debonding fractures with respect to various temperatures [24,30–34], however, little investigation is focused on the high-temperature range (up to 1000 °C), as required for multi-material and multi-layer structures, such as SOEC.

If debonding is defined as the failure of bonding forces for a variety of interfaces, delamination is a closely related problem of the material separation and fracturing specifically into layers. Both delamination and debonding could appear in layered structures of the same material composition and composed of different materials and can develop in a single-mode and a mixed-mode way. Delamination and debonding are studied in [35] for adhesively-bonded composite joints, in [36] – for sandwich shells with sensors and actuators, in [37] – for laminated composite plates. Prediction and suppression of delamination and debonding is discussed in [38,39], and migration of the delamination in composite laminates is modelled in [40] with the fragile points method. Another approach, cohesive zone model (CZM), is used for the combined problem of debonding and delamination in [41].

Delamination and its effects on the solid oxide electrolysis devices are reviewed by [42] and modelled by [43] using the geometry modifications. Experimental investigation into anode delamination is performed in [44], and the delamination mitigation and prevention in SOEC is studied in [45–47]. According to [48], SOEC performance is more sensitive to the delamination occurring at the centre of the electrolysis cell than at the edges. Optimisation strategy for the dynamic electrolysis process under conditions of a

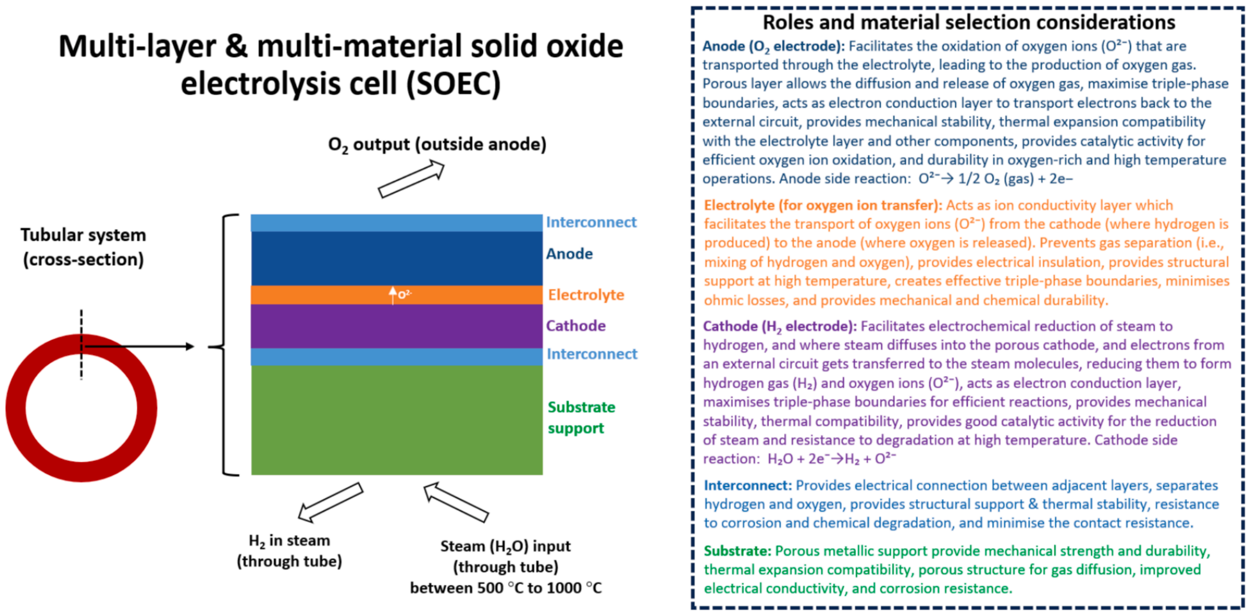

Fig. 1. Schematic showing multi-layer and multi-material solid oxide electrolysis cell (SOEC) system and illustrating some material selection considerations.

delaminating electrode is proposed in [49,50].

The cohesive zone model in fracture mechanics is a useful framework for fracture modelling with high accuracy across various materials, material heterogeneities, loading conditions, and crack paths. In this approach, a gradually growing fracture is considered, with the separation of surfaces at the crack tip. The cohesive zone refers to the space within the extending fracture, filled with the virtual material, allowing to describe cohesive forces acting on the separating surfaces. During separation, the modelled traction increases, reaching its' maximum, and then reduces to zero, indicating full separation of the surfaces. The cohesive zone model enables the simulation of crack branching, fragmentation, and near-tip behaviour [51]. The CZM approach is applied in fracturing simulations of carbon nanotube reinforced polymers [52], welded vessels [53], subsea pipelines [54], honeycomb core sandwich sheets [55], vulcanized rubber-metal bonding interface [56], laminated glass [57], composite laminated windshield [58], composite rigid double cantilever beam [59] and other laminated composites. It is considered good practice in research to obtain CZM parameters from dedicated experimental series to ensure simulation quality [60]. Several variations of the CZM method include mode-dependent [61], thermo-mechanical coupled [62] and generalised model formulations [63]. Uncertainty quantification of a rate-dependent CZM is demonstrated in [64] for polymer interfaces. Analytical solution for deformation is proposed based on the CZM model in the work by [65]. The impact of environmental conditions on mixed-adhesive joints is studied in [66]. In the work by [62], the CZM is applied to simulate temperatures up to 450 °K for the debonding process, while the research by [67] focuses on the subzero temperatures down to −20 °C. High temperature conditions up to 873 °K are considered in [68] for fracturing of hat-shaped specimens of the rail steel.

Analysis of the literature indicates a lack of research on the debonding phenomenon in high-temperature SOEC devices. The aim of the current study is to investigate the high-temperature (between 500 °C to 1000 °C) thermomechanical behaviour at interfaces with the cohesive zone model. The cell itself is constructed from several layers (assumed non-porous) made of multiple materials performing individual functions, detailed in the following section of the paper. Given the differences in thermal expansion coefficients of these materials, there is a high chance of interfacial failure due to debonding and consequent crack propagation.

2. Model

2.1. Structural model

The structural model used in this study is illustrated in Fig. 2 and is based on the paper [69], where a six-layer tubular SOEC is considered. The model includes five thin functional layers (two interconnects, a cathode, an electrolyte and anode), deposited on a thick titanium metallic support. The tubular cell model, which is assumed non-porous, is tested for the operational range of 500 °C to 1000 °C. The structure is subjected to an internal flow pressure load of 1 MPa, thermal loading and the effects of fixed boundary conditions. The fixed–fixed supports applied in the current study allow investigating the worst-case scenario debonding and

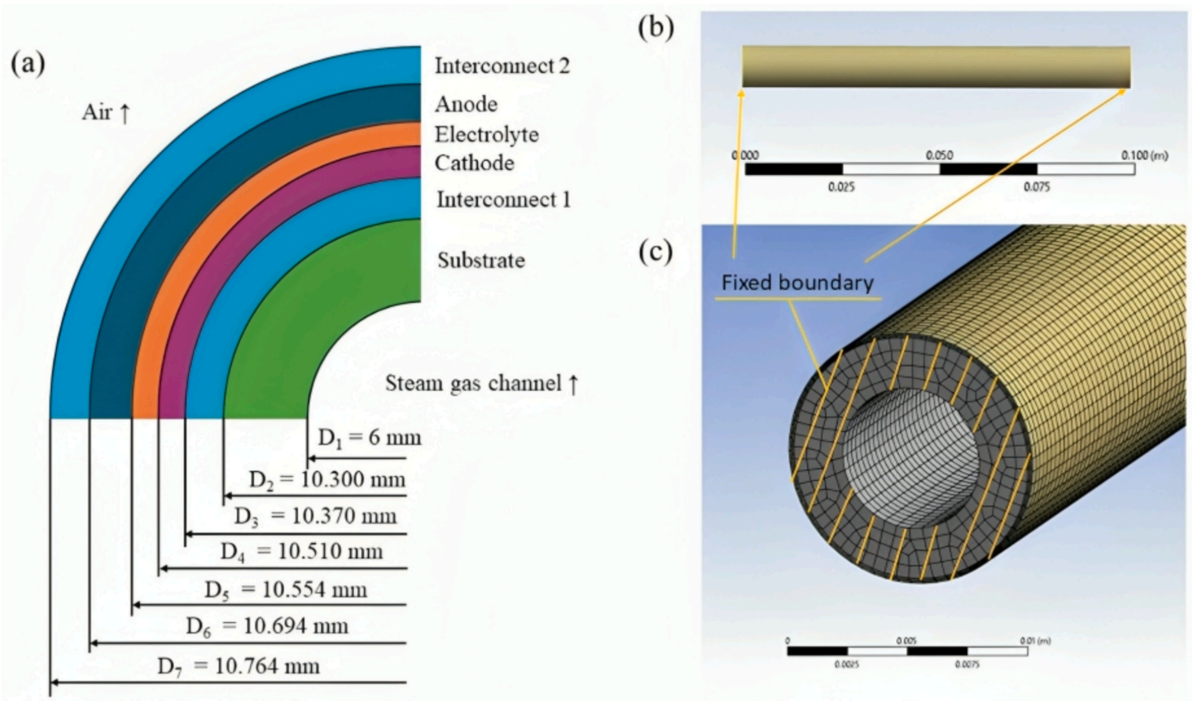

Fig. 2. Cross-section of six (non-porous) layers of the part of the tubular model: (a) general schematic of the cross-section; (b) structural model in Static Structural; (c) mesh of 90,762 elements.

deformation across the high-temperature range. The present work considers thermomechanical deformation for an improved material composition, compared to this previous research, closer to the SOEC fabricated, and the properties of the layers for the current simulation are shown in Table 1. Materials used include titanium alloy (Ti-6Al-4V), silver (Ag), nickel oxide (NiO), gadolinium-doped ceria (GDC), yttria-stabilised zirconia (YSZ) and lanthanum strontium cobalt ferrite (LSCF). The interfacial debonding is studied in the present work for five contact areas with the cohesive zone material model, described in the following subsection.

The total thickness of the model wall is 2.382 mm, including the substrate layer. The length of the structural model is 100 mm, as shown in Fig. 2(b). Due to the high aspect ratio of the five functional layers, including two interconnect layers, a cathode, an anode and electrolyte, these layers are modelled with shell elements, each having six degrees of freedom. At the same time, the substrate layer is meshed with solid elements, with three degrees of freedom each, as illustrated in Fig. 2(c). The thick substrate layer design of the SOEC is proposed in this study based on its potential for better mechanical strength, as is known for this type of support.

The current research considering the six-layer structure model is focused on the formation of debonding regions at the interfaces, estimated during the steady-state simulation in Static Structural. The basis for the Static Structural simulation is the displacement–-strain equation:

$$\varepsilon = [B]u. \tag{1}$$

Here, ε is the strain vector, $[B]$ stands for the matrix of shape functions for each element of the model, u is the nodal displacement vector.

Linked to Eq. (1), the stress–strain equation is:

$$\sigma = [D]\varepsilon, \tag{2}$$

where σ is the stress vector, and $[D]$ is the elasticity matrix, reflecting the material properties.

The Hooke's law is applied to link the displacement vector and the applied force f_a through the stiffness matrix $[K]$:

$$f_a = [K]u \tag{3}$$

Internal forces f_{int} acting on the structure are calculated as a volume V integral:

$$f_{int} = \int_V [B]^T \sigma dV \tag{4}$$

Internal and external forces f_{ext} on the structure are considered to be in balance, or:

$$f_{int} = f_{ext} \tag{5}$$

Solution in Static Structural is obtained with the Newton-Raphson method, which could be spelled for an arbitrary variable x, iteration m and function $f(x)$:

$$x_{m+1} = x_m - \frac{f(x_m)}{f'(x_m)}. \tag{6}$$

The Augmented Lagrange formulation is used for all contact areas, as advised by the ANSYS guidance [70] for debonding calculations. This formulation uses Lagrange multipliers to represent the contact forces and allows evaluating situations where contact between parts of the structure occurs or does not occur. This formulation is considered to be numerically stable and can be used for

Table 1
Material properties of six (non-porous) layers of the structural model.

Layer	Material(s)	Density, kg/m^3	Melting temperature, °C	Young's modulus, GPa	Poisson ratio	Thermal expansion coefficient, μm/m°C
Substrate tube	Titanium alloy (Ti-6AL-4V)	4405 [70,72]	1605 [70,72]	107 [70,72,82]	0.32 [70,72]	8.9 [70,72]
Interconnect 1 (Current collector 1)	Silver (Ag)	10,490 [70,72]	961 [79]	83 [80–82]	0.37 [70,72]	19 [70,72,82]
Cathode	0.6:0.4 NiO: GDC	6882 [83–86]	2273 [83,87]	151.2 [88–90]	0.33 [88–90]	12.1 [91,92]
Electrolyte	0.91:0.09 GDC: YSZ	7083 [84–86,93–95]	2745.5 [87,96,97]	128.1 [88–90,93,98]	0.26 [88–90,94,95,98]	11.4 [92–94,97,99]
Anode	0.5:0.5 GDC: LSCF	6600 [84–86,100–103]	1835 [87,103–104]	145 [89,90,101–105]	0.28 [89,90,103,105]	13 [92,101,106]
Interconnect 2 (Current collector 2)	Silver (Ag)	10,490 [70,72]	961 [79]	83 [80,81,82]	0.37 [70,72]	19 [70,72,82]

List of references for Table 1: [1] [70,72]; [2] [79]; [3] [80]; [4] [81]; [5] [82]; [6] [83]; [7] [84]; [8] [85]; [9] [86]; [10] [87]; [11] [88]; [12] [89]; [13] [90]; [14] [91]; [15] [92]; [16] [93]; [17] [94]; [18] [95]; [19] [96]; [20] [97]; [21] [98]; [22] [99]; [23] [100]; [24] [101]; [25] [102]; [26] [103]; [27] [104]; [28] [105]; [29] [106].

several types of contact, including bonded and frictional. The Augmented Lagrange formulation can be expressed as:

$$L_{aug} = L + \sum_i \lambda_i \phi_i + \frac{k}{2} \sum_i \phi_i^2, \tag{7}$$

where L is the original Lagrangian of the system, λ_i is an estimate of the Lagrangian multiplier, ϕ_i is the contact gap or penetration between the surfaces, i is the index of equality constraint, k is the penalty parameter, so that the third term penalizes the contact violations.

The Static Structural computational module in ANSYS provides a very flexible, versatile set of tools to simulate a wide range of structural conditions, including fractural simulations, realistic boundary conditions, diverse material properties, body interactions, pressure, temperature, other types of loads and custom, user-defined conditions. Static Structural allows coupling with other computational modules and supports the use of various specialized models, separately and in combination. The CZM model employed in the current research is an example of a specialised model, specifically tailored for interfacial failures. With all advantages, Static Structural simulations have some limitations, for instance, a high-resolution analysis can be demanding in terms of the computational resources. This may pose a limit on the level of detail when considering stress–strain conditions of complex objects and high aspect ratio structures.

2.2. Debonding model

The current study uses the CZM model [71–74], which was initially designed for simulating fractures and delamination, initiation, propagation and coalescence of cracks and debonding interfaces. The CZM model is applicable for composite materials, adhesively bonded joints, thin films and layered structures with multiple materials, that exhibit complex fracture processes. The CZM model is based on the traction-separation relationships, which represent the mechanical cohesive behaviour at the interface of adjacent material regions.

The mixed-mode bilinear cohesive zone material model derives the separation of material interfaces from both the normal and tangential components of displacement jumps. Here, a non-dimensional effective displacement jump λ reads as:

$$\lambda = \sqrt{\left(\frac{\delta_n}{\delta_n^c}\right)^2 + \beta^2 \left(\frac{\delta_t}{\delta_t^c}\right)^2}, \tag{8}$$

where β is the non-dimensional parameter of scaling (weighting) the tangential component of displacement δ_t, and δ_n is the normal component of displacement jump, while δ_n^c and δ_t^c are the normal and tangential displacement jumps at the completion of debonding.

The interfacial separation δ in general is the displacement jump or the difference of displacements of the adjacent interface surfaces u^{top} and u^{bottom}:

$$\delta = u^{top} - u^{bottom}. \tag{9}$$

Therefore, the normal displacement is the normal separation in the local direction $\boldsymbol{n}$, and the tangential displacement is the tangential separation in the local direction of $\boldsymbol{t}$:

$$\delta_n = \boldsymbol{n} \bullet \delta, \tag{10}$$

$$\delta_t = \boldsymbol{t} \bullet \delta. \tag{11}$$

The normal cohesive traction T_n is linked through the normal cohesive stiffness K_n and the damage parameter D_m to the normal displacement jump as follows:

$$T_n = K_n \delta_n (1 - D_m) \tag{12}$$

Here, the normal cohesive stiffness depends on the maximum normal cohesive traction T_n^{max} and the normal displacement jump at the maximum normal cohesive traction δ_n^*:

$$K_n = \frac{T_n^{max}}{\delta_n^*} \tag{13}$$

The damage parameter D_n is defined as:

$$D_n = \begin{cases} 0, at \lambda^{max} \leq \lambda_{cr} \\ \min(1, d_m), at \lambda^{max} > \lambda_{cr} \end{cases}, \tag{14}$$

where λ^{max} is the maximum of the λ history, λ_{cr} is the value of λ at which the maximum effective traction occurs, and the d_m coefficient is spelled as

$$d_m = \eta \left(\frac{\lambda^{max} - \lambda_{cr}}{\lambda^{max}} \right), \tag{15}$$

where the η coefficient is

$$\eta = \frac{\delta_n^c}{\delta_n^c - \delta_n^*} = \frac{\delta_t^c}{\delta_t^c - \delta_t^*}, \tag{16}$$

where δ_t^* is the tangential displacement jump at maximum tangential cohesive traction. The critical value of λ_{cr} is defined as:

$$\lambda_{cr} = \frac{\delta_n^*}{\delta_n^c} = \beta\frac{\delta_t^*}{\delta_t^c}, \tag{17}$$

The tangential component T_t of the cohesive traction in the mixed mode version of the bilinear model reads as:

$$T_t = K_t\delta_t(1 - D_m), \tag{18}$$

where K_t is the tangential cohesive stiffness, or

$$K_t = \frac{T_t^{max}}{\delta_t^*}, \tag{19}$$

where T_t^{max} is the maximum tangential cohesive traction.

Additionally, the ratio of $\alpha = \delta_n^*/\delta_n^c$ is referred to as the artificial damping coefficient.

The current simulation uses coefficients for the separation-distance-based debonding: $T_n^{max} = 45$ MPa, $\delta_n^c = 1\mathrm{e}{-6}$ m, $T_t^{max} = 45$ MPa, $\delta_t^c = 1\mathrm{e}{-6}$ m, and $\beta = 2$. Here, T_n^{max} and T_t^{max} are obtained from the literature [75–78], and δ_n^c and δ_t^c are selected based on the preliminary simulations in order to resolve the fracture. All interfaces have the same CZM settings.

The CZM model is a high-resolution method, which allows looking into the intriguing nature of interfacial failures in detail. However, using the model in Static Structural analysis requires an incremental, stepwise load application during the standard 1 s time step and a high accuracy mesh, as discussed in the following subsection.

2.3. Mesh analysis and verification of the structural model

The mesh analysis for thermal expansion without the fracture is verified, as in Fig. 3, in terms of the maximum total deformation. An unstructured mesh is used for both solid and shell elements. A mesh consisting of 90,762 cells was initially selected, delivering a maximum total deformation of about 8.5e-5 m for the considered model at 800 °C. Further simulations with the mesh of 90,762 cells demonstrated multiple solution convergence issues, when the debonding process is considered in the targeted range of temperatures. These were deemed to be due to higher element sizes leading to larger displacement jumps leading to instabilities in force convergence during the iterative solution process. For this reason, all simulation results in this work are reported for the mesh of 141,211 cells, with which a convergent solution was achieved.

Here the multi-layer and multi-materials system being studied is complex to model analytically. The intention of the current work is

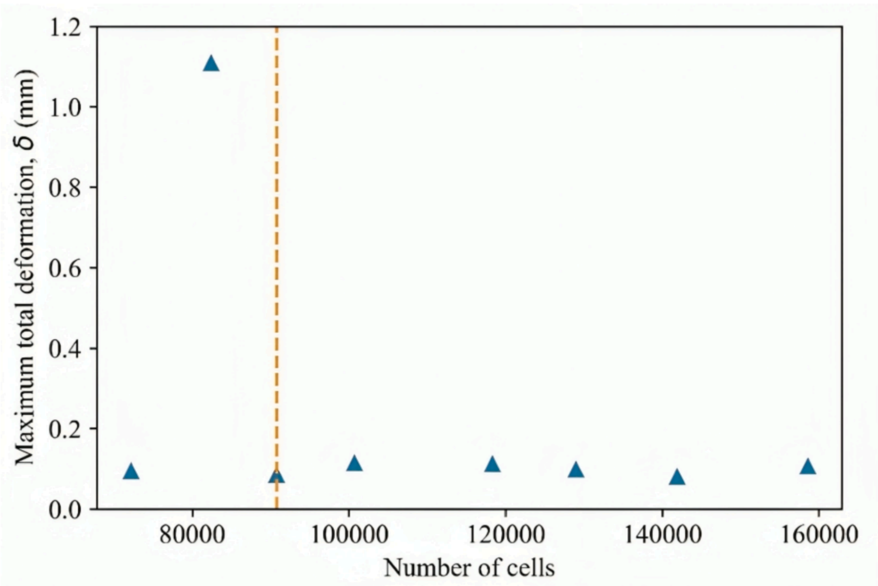

Fig. 3. Mesh independence test in terms of the maximum total deformation of the model with no debonding for 800 °C.

to investigate the specific design with the future vision to investigate it experimentally. As this investigation explores new phenomena, the simulation could serve as a preliminary investigation to guide future theoretical developments or experimental designs. The simulation also provides meaningful insights that align with expected physical behaviour and still can be valuable despite the lack of direct validation.

3. Results

3.1. Stress analysis

Debonding simulations in the temperature range from 500 °C to 1000 °C are performed with the increment of 50 °C, or 11 simulations in total. The results demonstrate relatively uniform (along the length of the cell) shear stress distributions for the substrate and outer layers, as shown in Fig. 4 for the borders of the considered temperature interval. The immediate effect of the fixed boundary conditions is observed near both ends in the contours of normal stresses at 500 °C, as appears in Fig. 4 for the substrate layer. A similar circular stress change is observed around the fixed boundary in the 6th layer at 500 °C, although these results are not shown in the paper for brevity. Normal stresses also exhibit belt-shaped concentrations near the fixed boundaries for 1000 °C. A high concentration of the radial stress and of the hoop stress at 1000 °C propagates into the body of the substrate, which hints to the location of debonding regions in the tubular cell. At the same time, the largest stress above 1 GPa is the shear XY stress at 1000 °C at the substrate's fixed boundary. Failure initiation and propagation are expected to occur well before the shear stress reaches this high value.

The high temperature impact on the normal and shear stresses is illustrated in Fig. 5(a–f) for the 50 mm mark (i.e., the midpoint of the 100 mm-long tubular SOEC, Fig. 5(g)). The data are presented for the X coordinate for the full thickness of the cell model (Fig. 5(h)). As comes from Fig. 5, a principal transition to a fully formed crack between 600 °C and 800 °C is significant in the radial stress in the substrate, as in Fig. 5(a), and in the shear XY and XZ stresses in the substrate, as in Fig. 5(b) and (f). A large jump in the shear YZ and XZ stresses at 1000 °C is observed in the thin layers in Fig. 5(d) and (f). A notable rise in longitudinal stress occurs between the temperatures of 800 °C and 1000 °C for both the supporting substrate and thin functional layers. The longitudinal stress on the border with thin layers in Fig. 5(e) is the largest among all the stresses, experienced by the structure. The hoop stress magnitude in Fig. 5(c) is relatively low in the substrate and high in the thin layers, and changes among the temperatures appear to be less pronounced.

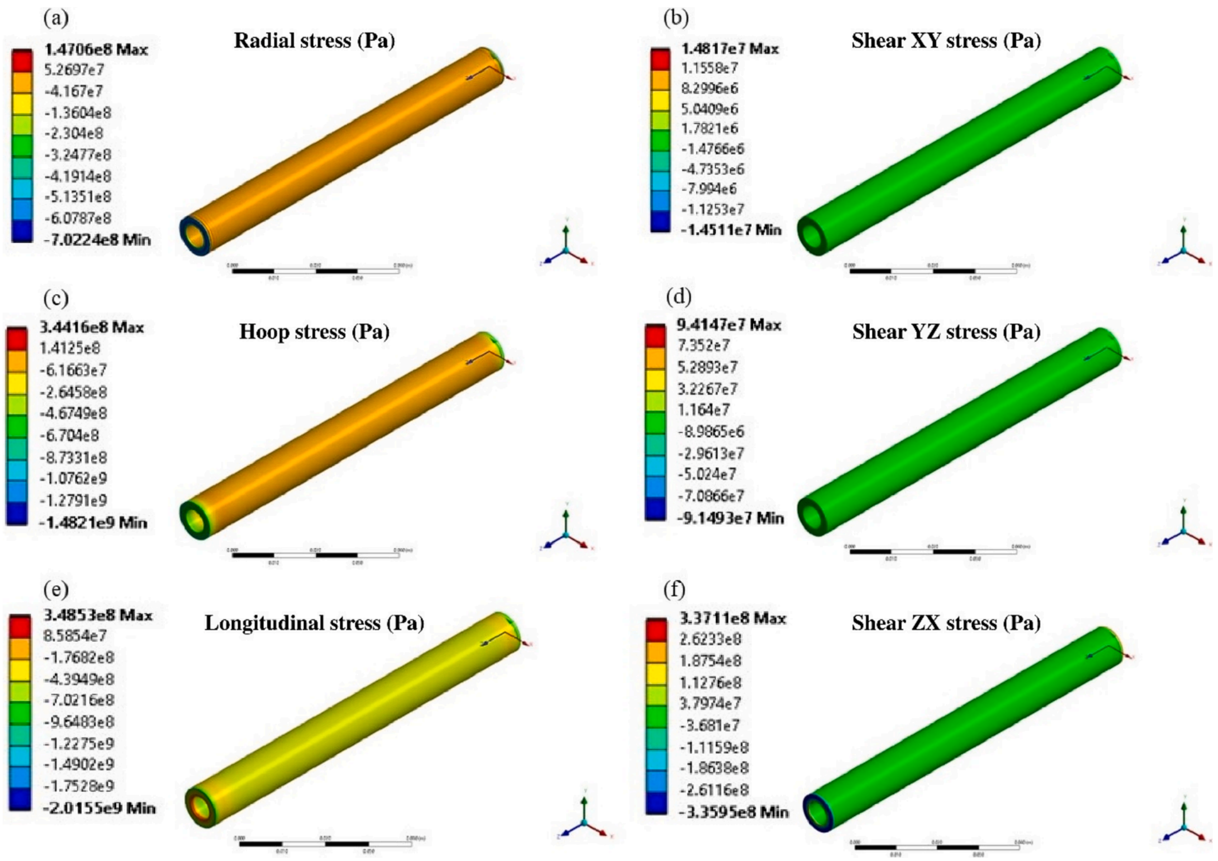

Fig. 4. Example stresses of the model exhibiting debonding for the substrate at 500 °C: (a) radial stress; (b) shear XY stress; (c) hoop stress; (d) shear YZ stress; (e) longitudinal stress; (f) shear ZX stress (stresses in Pa, length scale bars: 0.06 m).

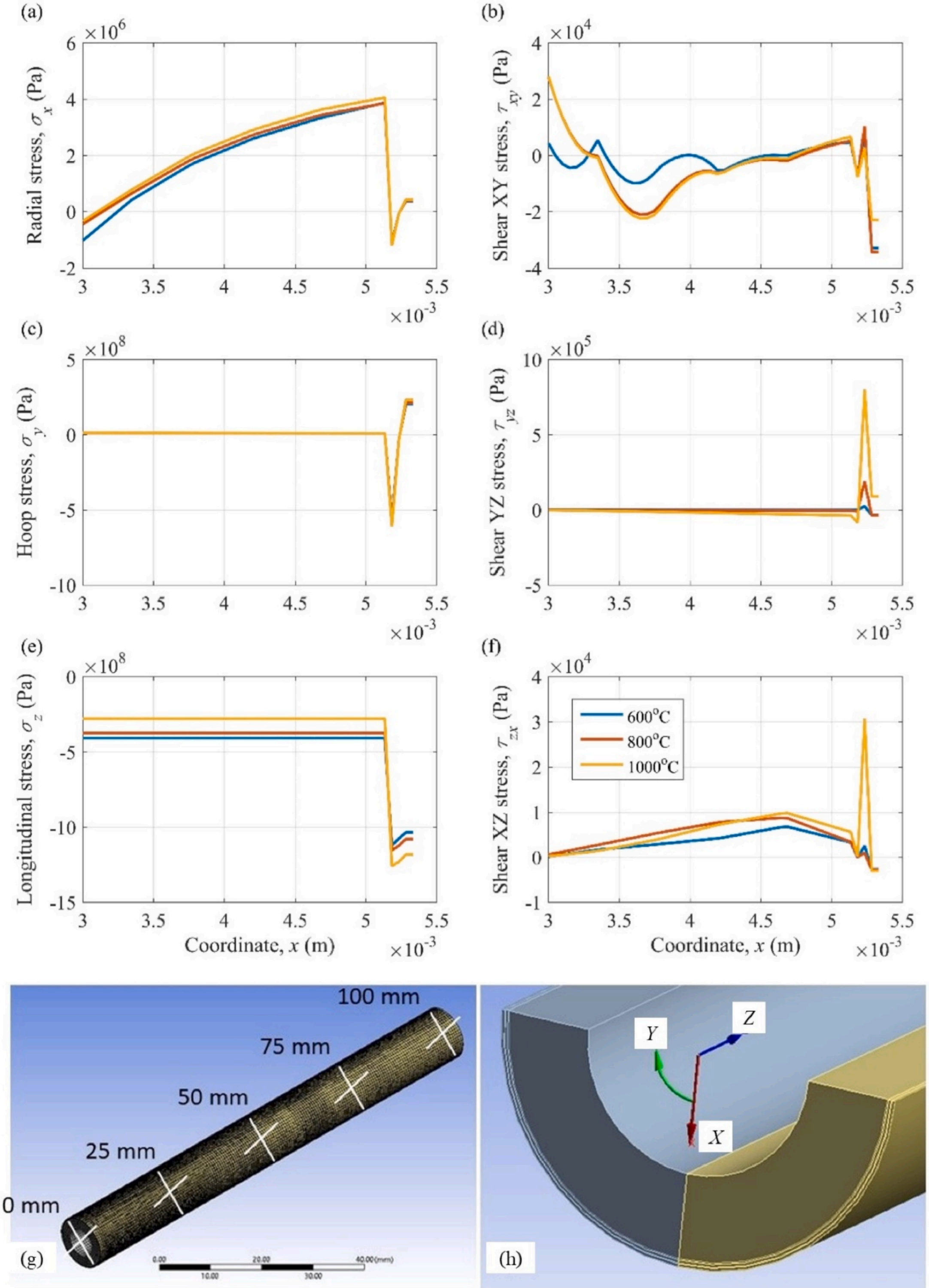

Fig. 5. High temperature (600 °C, 800 °C, and 1000 °C) effect on the model exhibiting debonding in terms of the stresses in the middle of the structure (50 mm mark, i.e., at middle of the 100 mm long tubular SOEC cell, in the positive direction of X axis): (a) radial stress; (b) shear XY stress; (c) hoop stress; (d) shear YZ stress; (e) longitudinal stress; (f) shear ZX stress; (g) representative cross-sections along the length of SOEC; (h) coordinate system.

3.2. Deformation analysis

Analysis of the total deformation at 500 °C indicates belt-shaped changes in the deformation contours for all six layers, as appears in Fig. 6. This pattern is consistent with the contours of normal stresses, displayed in the previous subsection. The total deformation is otherwise uniform for the first and second layers, shown in Fig. 6(a) and (b), while all other layers exhibit two zones of either increased or decreased deformation. The maximum total deformation in this case is 0.061 mm and is observed in the midsection of the structure in the outer layer, in the red zone in Fig. 6(f).

The total deformation contours significantly change, when the SOEC structural model with the debonding process is heated to 1000 °C, as appears in Fig. 7. Here, the substrate layer shows belt-shaped low-deformed zones near fixed boundaries. In Fig. 7(b), the second layer of the cell demonstrates belt-shaped zones of decreased and increased deformation. Layers 3 and 4 in Fig. 7(c) and Fig. 7(d) have two elongated zones of decreased and increased deformation along the body of the cell, and up to eight deformation zones around each fixed boundary. These deformation zones are present but less pronounced in layers 5 and 6 in Fig. 7(e) and (f). The maximum total deformation in the model reaches 0.128 mm at 1000 °C, against the level of 0.061 mm at 500 °C, or twice as high. This significantly increases the risk of fracturing at the interfaces, especially for layers 3 and 4.

The heat accumulated in the tubular cell above 600 °C causes the structure to exhibit multiple deformation patterns, that are also indicated for the full model in Fig. 8 across the considered temperature range. The process begins at about 650 °C, as in Fig. 8(c), together with the formation of fully developed debonding areas. Fig. 8(c–f) indicate that deformation zones are pronounced near the fixed boundary and are asymmetric in terms of the deformation magnitude values across the structure. The result in Fig. 8(d) not only indicates the maximum total deformation in the tests but also reveals the clear presence of eight deformation zones at each boundary and four such zones in the middle section of the tubular cell. Contours in Fig. 8(c), (e), and (f) demonstrate similar deformation patterns (general asymmetry and same number of deformation zones). Fig. 8(a) suggests that in the range of 500 °C to 600 °C, where the debonding initiation only is observed, the maximum total deformation follows almost a linear growth, increasing with the temperature. This corresponds to the "Near" debonding fracture status. Formation of a fully open crack at 650 °C and higher in the temperature range leads to a slightly unpredictable trend in the expected maximum total deformation, limited by the observed highest

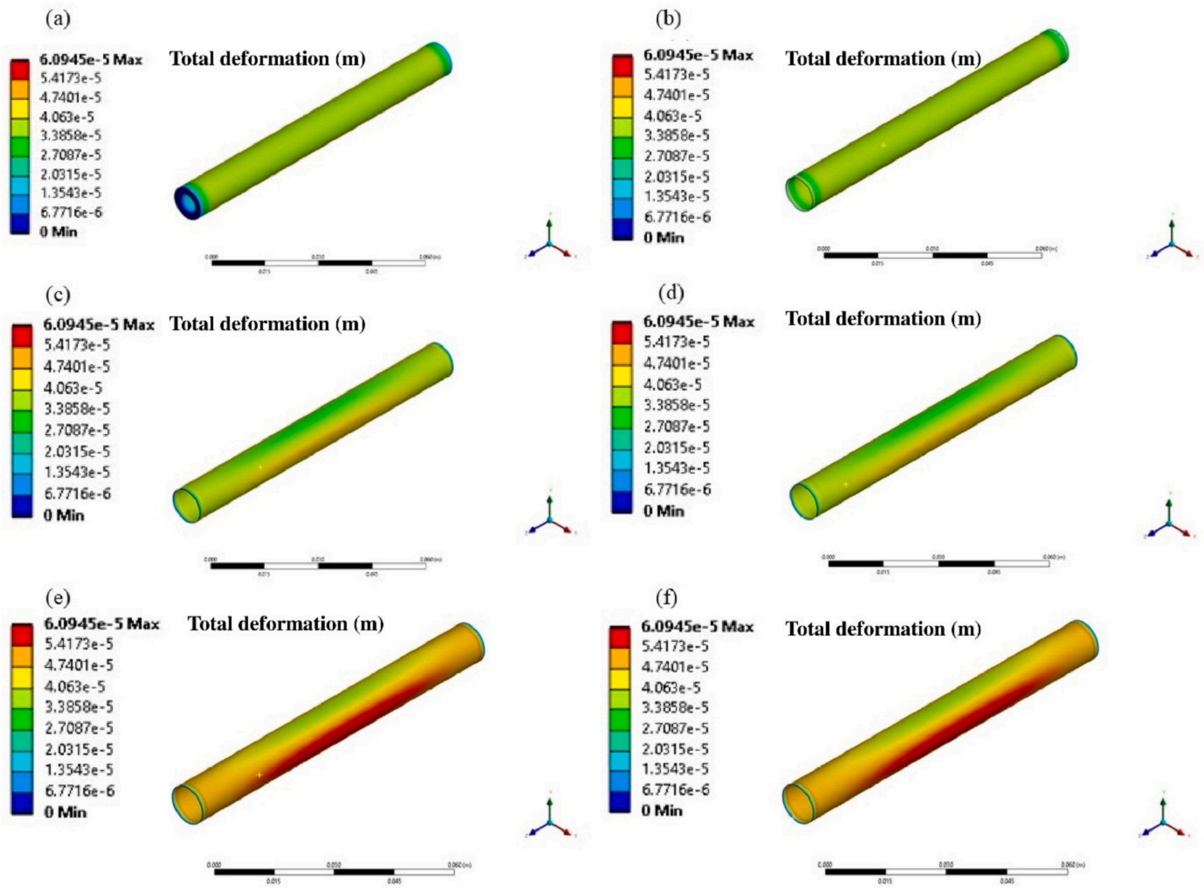

Fig. 6. Example total deformation contours for six layers of the structural model at 500 °C: (a) first layer; (b) second layer; (c) third layer; (d) fourth layer; (e) fifth layer; (f) sixth layer (deformation in meters, length scale bars: 0.06 m).

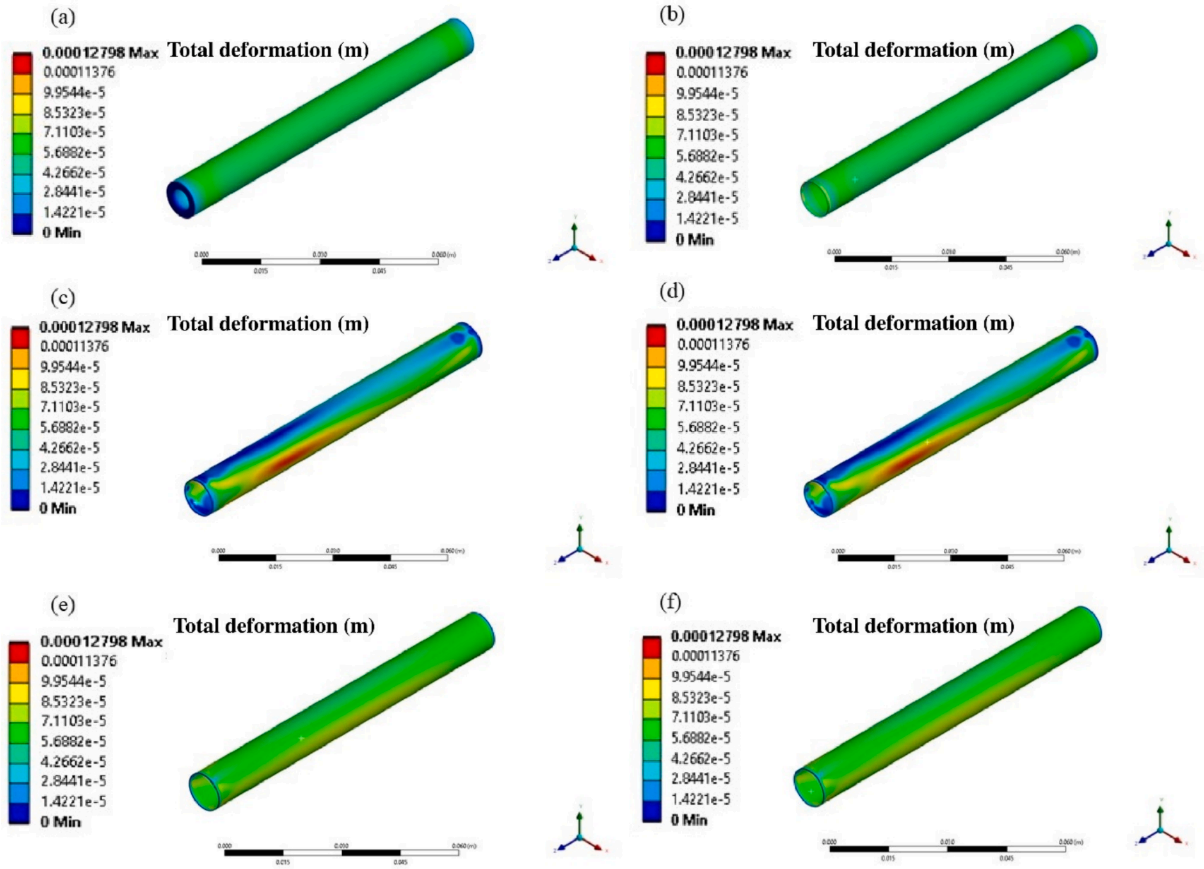

Fig. 7. Example total deformation contours for six layers of the structural model at 1000 °C: (a) first layer; (b) second layer; (c) third layer; (d) fourth layer; (e) fifth layer; (f) sixth layer (deformation in meters, length scale bars: 0.06 m).

value of 0.244 mm at 750 °C. This corresponds to the "Far" debonding fracture status. The maximum deformation observed at 750 °C indicates the highest risk of fracturing in the structure in the operating temperature range.

3.3. Fracture propagation

Debonding process in this work is generally tracked as the thermal load is incremented gradually, limited by a maximum of 100 steps. The evolution of the process can be traced through the changing sliding distance variable, illustrated in Figs. 9–11. Fig. 9(a) specifically illustrates the early fracture formation, visible during the steady-state simulation, where the debonding process initiates around the circular fixed boundary, and this region expands from 500 °C to 600 °C. At the same time, the maximum total deformation increases for about 30 % between these temperatures. Transition of the debonding initiation to a fully formed crack occurs between 650 °C and 700 °C, where the debonding process takes place in the area around the fixed boundary, as well as propagates deeper into the body of the tubular cell. This is consistent with significant changes in the interlayer sliding distance (tracked for the interfaces) around the fixed boundary, seen in Fig. 9(b) for 700 °C, and the peak maximum total deformation in Fig. 8(a), which exceeds values observed at both lower and higher temperatures. Propagation of the debonding fracture to nearly the middle of the cell is evident from Fig. 9(c) and (d) for 900 °C and 1000 °C respectively, for the first interface between the substrate and the second layer of the model.

Debonding fracturing into the body of the cell is further analysed through changes at the third interface (between the third and fourth layers of the model), displayed in Fig. 10, and the fifth interface (between the fifth and the sixth layers of the model), displayed in Fig. 11. Both high and low sliding distances are observed propagating into the body of the cell in Fig. 10, starting at a temperature of 700 °C, and this process is not symmetric relatively the middle of the cell. The result in Fig. 10(d) for 1000 °C, showing high variation in sliding distances at the third interface, is consistent with the high variation in total deformation seen in layers 3 and 4 in Fig. 7(c) and (d). Similar sliding distances across the cell body are observed at the fifth interface, but they are more pronounced at 700 °C and less pronounced at 900 °C and 1000 °C. This trend aligns with the overall lower level of deformation, seen in Fig. 8(a).

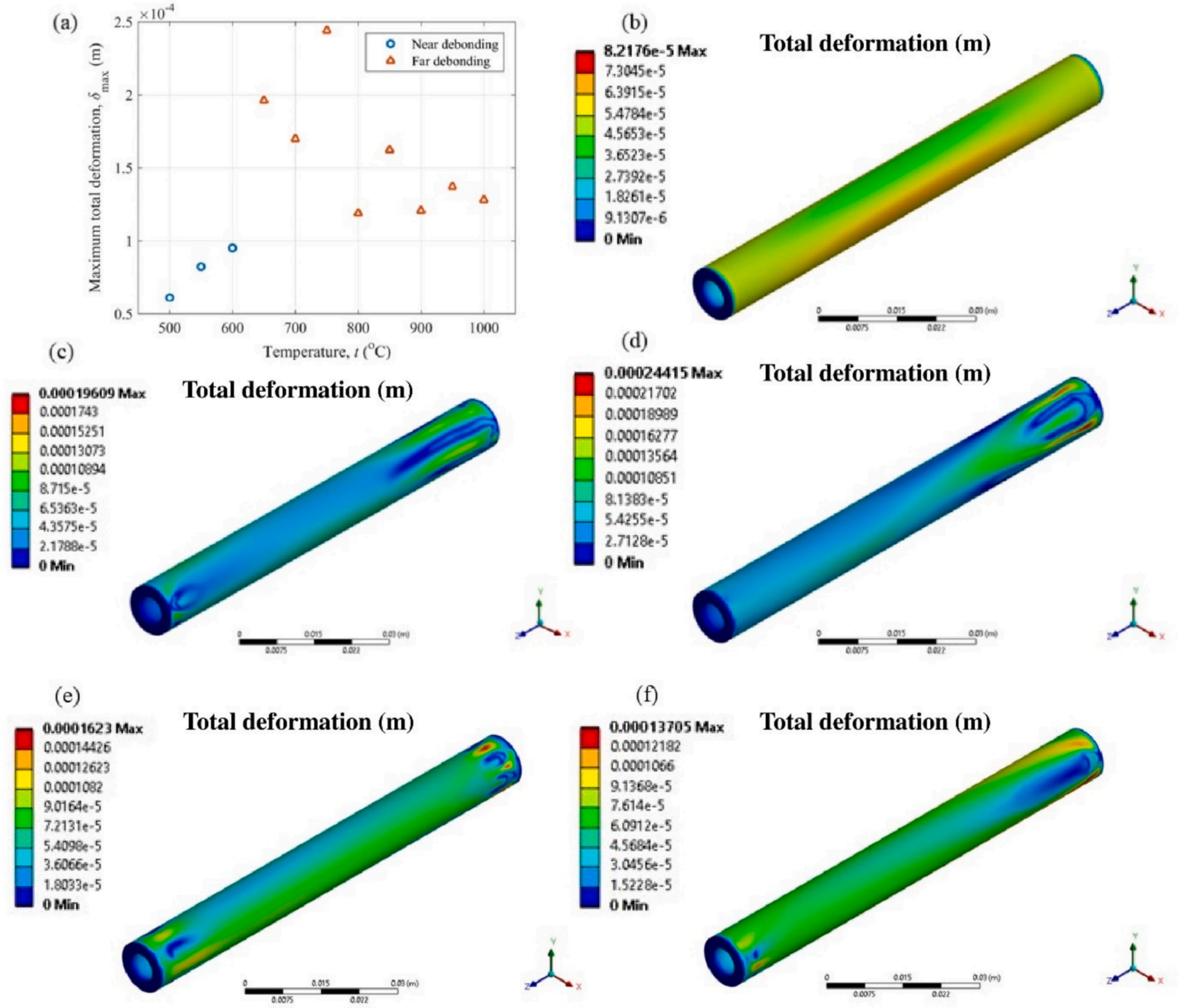

Fig. 8. Total deformation changes with the temperature increase: (a) maximum total deformation statistics across the range of 500–1000 °C; contours of the total deformation for the full structure at (b) 550 °C, (c) 650 °C, (d) 750 °C, (e) 850 °C, (f) 950 °C (deformation in meters, length scale bars: 0.03 m).

4. Discussion

As can be seen in Figs. 4–11, there is a marked variation in deformation, stress, debonding distribution through the multi-material and multi-layer tubular structure subjected to internal pressure. This gets more extreme as the temperature rises. As expected, the multi-material and multi-layer tubular structure undergoes significant deformation where different materials deform differently under the applied model settings. The irreversible deformation is more pronounced at high temperatures, as in Fig. 8, due to thermal softening, which reduces the yield strength of the materials. At high operating temperatures, each layer's material expands differently, and this expansion can induce complex stresses, especially if layers of the tubular structure have different thermal expansion coefficients. High temperatures are expected to exacerbate interfacial debonding by causing differential expansion, and areas with high-stress concentrations are especially prone to debonding. Cracks are likely to initiate in regions where stresses are high, and once cracks are initiated, they can propagate through the thickness of the multi-layer tubular structure. It is important to note that debonding can interact with cracks and can serve as pathways for crack propagation and leading to delamination and spalling within the structure. Overall, the CZM model can simulate the initiation and propagation of debonding and cracking at the interfaces, enabling a comprehensive analysis of the multi-layer tubular structure.

Consideration of debonding in the non-porous cell model leads to the results different from those observed in [69], where no fractures were simulated. Thus, it can be suggested that debonding suppresses the areas of the high deformation seen in [69] along the body of the tubular cells, however, substantially amplifies processes near the fixed boundaries, manifesting in high deformations, multiple deformation shapes, stress fluctuations and fractures. This behaviour is primarily attributed to the allowance of differential

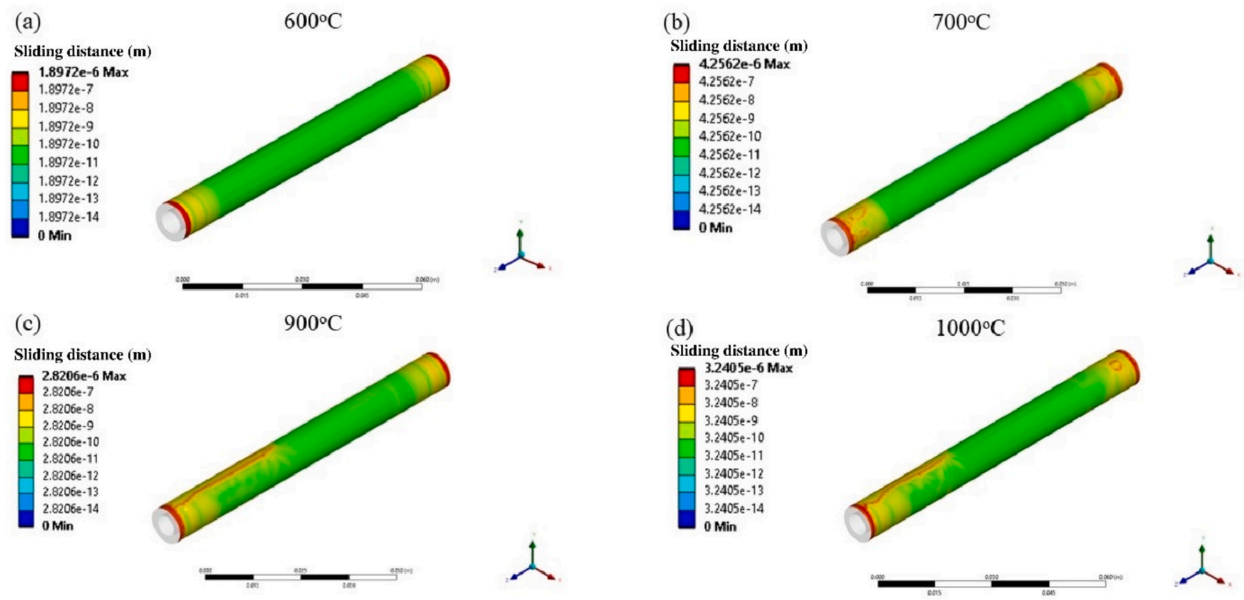

Fig. 9. Contours of the sliding distance at the first interface of the substrate layer and the second layer at: (a) 600 °C; (c) 700 °C; (c) 900 °C; (d) 1000 °C (contour in meters, length scale bars: 0.06 m).

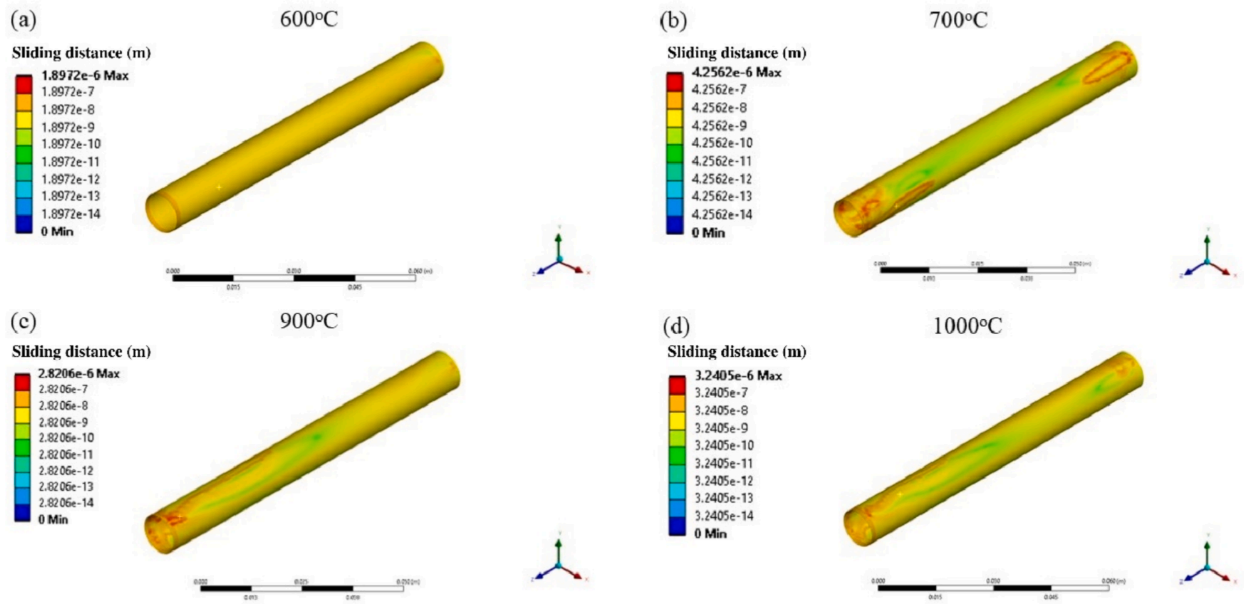

Fig. 10. Contours of the sliding distance at the third interface of the third layer and the fourth layer at: (a) 600 °C; (c) 700 °C; (c) 900 °C; (d) 1000 °C (contour in meters, length scale bars: 0.06 m).

deformation across the interfaces enabled by the definition of the interfaces. These interfaces behave like deformable springs which allow relative thermal expansion thus accommodating any bulk deformation until a critical threshold is reached. At the same time, both studies indicate formation of belt-like zones near fixed boundaries seen in deformation (as in Fig. 6(e) and (f)) and stress (e.g. Fig. 4(e)) contours, and abrupt changes between stress values found in the thck substrate and thin functional layers.

An important finding of the current research is the observation of clear multiple deformation shapes, where up to eight zones (Fig. 7, Fig. 8) are seen close to a boundary and two to four zones of deformation form along the body of the structure. These zones are identified as areas of potential debonding, fracture and crack growth. It should be noted that the interfacial bond strength characteristics across the different layers play a critical role in determining the overall structural integrity of the tubular cell. Therefore, experimental determination of the interfacial strength and toughness is critical for calibrating the CZM model parameters leading to

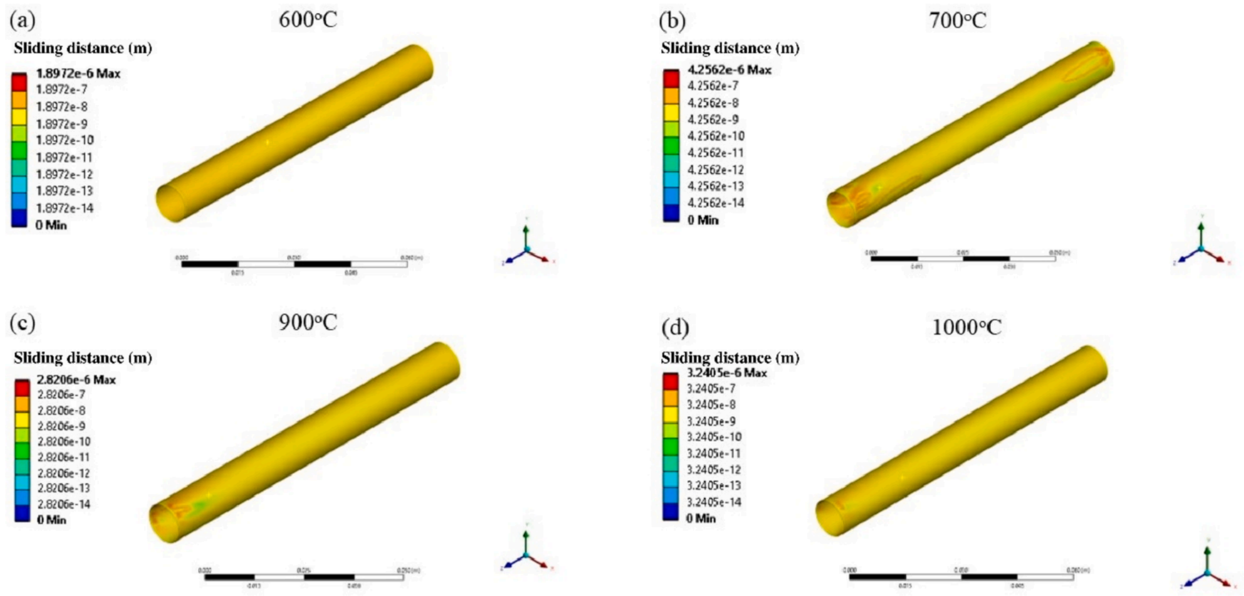

Fig. 11. Contours of the sliding distance at the fifth interface of the fifth layer and the sixth layer at: (a) 600 °C; (c) 700 °C; (c) 900 °C; (d) 1000 °C (contour in meters, length scale bars: 0.06 m).

realistic predictions of the high temperature behaviour of the proposed tubular cell design. Furthermore, the effect of porosity across the different layers, which plays a critical role in the chemical species transport, also needs to be thoroughly investigated to understand its impact on the thermo-mechanical behaviour.

It is important to emphasise, that debonding has a critical effect on the intensity and location of chemical reactions within SOEC. Although the primary cause of debonding in SOEC is linked to the thermal expansion mismatch among thin layers of the cell under high-temperature conditions, accelerated by thermal cycling, chemical reactions during electrolysis may also lead to an intensification of debonding failure at interfaces. The first chemical factor weakening the interfaces is the accumulation of oxygen atoms and reduction–oxidation cycling, both acting as a source of internal stresses within the materials. The second factor reducing adhesion strength from the chemical side is reactions between the electrode and electrolyte materials and reactions with possible contaminants of the steam. The third factor promoting debonding comes from possible species of interconnect materials, which may deposit on the electrodes during cell operation in real-world conditions. The mutual influence of debonding processes and chemical reactions presents a compelling subject for future research in this area.

The results obtained in the current paper provide a foundation for further investigations into the fracturing of solid oxide electrolyser structures, complementing the studies [16,42–46], which primarily focus on delamination. The analysis of debonding, delamination and other types of fractures is of outmost importance for the technology based on the high temperature process. In a multi-layer and multi-material tubular structure, fracture may initiate at sites of high stress concentration, such as interfaces between layers, defects, or areas of material heterogeneity. By incorporating thermal expansion and damage evolution into the cohesive zone framework, the CZM becomes a powerful tool for predicting structural degradation in materials exposed to complex thermomechanical loads.

Additionally, material and manufacturing considerations (as outlined by the roles of various layers illustrated in Fig. 1) should prioritize thermal stability, high-temperature strength, and compatibility with adjacent layers to minimise their inter-layer debonding. While the fabrication of multi-layer and multi-material tubular structure is considered as part of future work, the integration of CZM into both the design phase and the manufacturing process is expected to be essential for producing high-performance SOEC structures. However, challenges remain in applying CZM to tubular SOEC structures. These challenges comprise the need for detailed knowledge of multi-material properties (cohesive strength, fracture toughness, energy release rates), assessment of mesh sensitivity, consideration of material non-linearities of (e.g., plasticity, viscoelasticity, temperature-dependent properties), including any residual stresses in multi-layer structures.

5. Conclusions

Solid oxide electrolyser technology plays a significant role in the vision of the future transition towards a sustainable and carbon–neutral energy landscape. Structural analysis is crucial for evaluating novel SOEC designs at the cell level, including forecasting deformations, stress–strain conditions, and crack manifestation under high-temperature operating conditions.

The current study uses the cohesive zone model, incorporated into a finite element model of the tubular SOEC, to obtain reliable predictions of potential crack occurrences. CZM models encapsulate the mechanical behaviour at material interfaces through cohesive laws, and the present study is considering specifically the formation of debonding regions, due to multiple material zones in the proposed SOEC design. The research stages include developing a six layers (non-porous) cell model, implementing custom material properties, performing a mesh test, simulating the diverse debonding process.

Main findings from this study include a temperature-dependent curvature for the maximum of expected total deformations, where a linear growth pattern transitions to a random pattern, with a peak value observed at 750 °C in the range from 500 °C to 1000 °C. Up to eight deformation zones which could potentially be crack initiation locations are found near the fixed boundaries in this study, and up to four zones are indicated by deformation contours along the main body of the tubular cell model. Finally, this study predicts that debonding is likely to occur during laboratory experiments of the proposed model, starting at temperatures around 650 °C near the fixed tubular end boundaries.

CRediT authorship contribution statement

Victoria Kurushina: Writing – original draft, Visualization, Validation, Software, Resources, Methodology, Investigation, Formal analysis, Data curation, Conceptualization. **Anil Prathuru:** Writing – review & editing, Supervision, Software, Resources, Methodology, Investigation, Funding acquisition, Formal analysis, Conceptualization. **Ajith Soman:** Writing – review & editing, Funding acquisition. **Mamdud Hossain:** Writing – review & editing, Funding acquisition. **Qiong Cai:** Writing – review & editing, Funding acquisition. **Bahman Amini Horri:** Writing – review & editing, Funding acquisition. **Nadimul Haque Faisal:** Writing – review & editing, Supervision, Software, Resources, Project administration, Methodology, Investigation, Funding acquisition, Formal analysis, Data curation, Conceptualization.

Declaration of competing interest

The authors declare that they have no known competing financial interests or personal relationships that could have appeared to influence the work reported in this paper.

Acknowledgments

The authors acknowledge high temperature steam electrolysis related funding by the UKRI EPSRC via Grants No. EP/W033178/1 (METASIS). Authors (NF, AP, MH) acknowledges thermochemical electrolysis related funding by UK National Nuclear Laboratory (NNL) via gamechanger Grant No. GC 596 (THERMOSIS). VK would like to acknowledge the support of the National Project "Science and Universities" of the Ministry of Science and Higher Education of the Russian Federation, grant number FEWN-2024-0005.

Data availability

Data will be made available on request.

References

[1] Banerjee A, Wang Y, Diercks J, Deutschmann O. Hierarchical modeling of solid oxide cells and stacks producing syngas via H2O/CO2 Co-electrolysis for industrial applications. Appl Energy 2018;230:996–1013.
[2] Mougin J. Hydrogen production by high-temperature steam electrolysis. In Compendium of Hydrogen Energy. Elsevier; 2015. p. 225–53.
[3] Stoots CM, O'Brien JE, Condie KG, Hartvigsen JJ. High-temperature electrolysis for large-scale hydrogen production from nuclear energy–experimental investigations. Int J Hydrogen Energy 2010;35(10):4861–70.
[4] Buttler A, Spliethoff H. Current status of water electrolysis for energy storage, grid balancing and sector coupling via power-to-gas and power-to-liquids: a review. Renew Sustain Energy Rev 2018;82:2440–54.
[5] Broek D. The practical use of fracture mechanics. Springer Science & Business Media; 2012.
[6] Gdoutos EE. Fracture mechanics criteria and applications, vol. 10. Springer Science & Business Media; 2012.
[7] Zehnder AT. Fracture mechanics, vol. 62. Springer Science & Business Media; 2012.
[8] Ritchie RO, Liu D. Introduction to fracture mechanics. Elsevier; 2021.
[9] Gdoutos EE. Fracture mechanics: an introduction, vol. 263. Springer Nature; 2020.
[10] Zhang F, Huang Q-A, Tang Z, Li A, Shao Q, Zhang L, et al. A review of mechanics-related material damages in all-solid-state batteries: mechanisms, performance impacts and mitigation strategies. Nano Energy 2020;70:104545.
[11] Yang C, Liu L, Liu Z, Huang Y, Yu S, Fu Y. Study on the mechanism of bond strength generation and debonding failure between basalt fiber and asphalt based on molecular dynamics. Case Stud Constr Mater 2023;19:e02493.
[12] Jiao B, Chen J, Gong M. Investigation of interfacial degradation mechanism and debonding behavior for degraded rubber asphalt-aggregate molecular system using a molecular dynamics method. J Clean Prod 2024;451:142123.
[13] Teng J, Fernando D, Yu T. Finite element modelling of debonding failures in steel beams flexurally strengthened with CFRP laminates. Engng Struct 2015;86:213–24.
[14] Siorikis D, Rekatsinas C, Chrysochoidis N, Saravanos D. Progressive debonding analysis of sandwich composite strips using a cohesive-layerwise spectral finite element model. Int J Solids Struct 2022;243:111560.
[15] Liu W-H, Kai M-F, Zhang P, Yu T, Dai J-G. Three-dimensional finite element modeling of debonding failure of skew FRP-bonded concrete joints. Engng Struct 2024;303:117537.
[16] Fan Y, Chen Y, Abernathy H, Pineault R, Addis R, Song X, et al. Enabling durable hydrogen production and preventing the catastrophic delamination in the solid oxide electrolysis cells by infiltrating SrFe2O4-δ solutions into LSM/YSZ-based air electrode. J Power Sources 2023;580:233389.
[17] Yang D, Sun Y, Zhou J, Wei G, Guan Z, Chen X. A multiscale interfacial cyclic debonding model for fibre-reinforced composites using micromechanics and molecular dynamics. Compos Struct 2024;330:117831.
[18] Martin E, Leguillon D. A strain energy density criterion for the initiation of edge debonding. Theor Appl Fract Mech 2015;79:58–61.

[19] Chen B, Zheng J, Chen Z, Tang Y, Ye Z, Wu C, et al. Quantitative analysis of debonding gaps in concrete-filled steel tubes on the Qinghai-Tibet Plateau under severely harsh conditions. Engng Struct 2024;314:118353.
[20] Bocciarelli M, Colombi P, Fava G, Sonzogni L. Energy-based analytical formulation for the prediction of end debonding in strengthened steel beams. Compos Struct 2016;153:212–21.
[21] Bruno D, Greco F, Feudo SL, Blasi PN. Multi-layer modeling of edge debonding in strengthened beams using interface stresses and fracture energies. Engng Struct 2016;109:26–42.
[22] Wu K, Lin S, Xu C, Chen C, Chen F. Energy dissipation and debonding mechanism of steel and steel fibre reinforced concrete composite beams. Engng Struct 2021;226:111353.
[23] Xue P, Wei X, Li Z, Wang Y, Selivanov MF, Xiong J. Mechanics of inner core debonding of composite sandwich beam with CFRP hexagonal honeycomb. Int J Solids Struct 2024;293:112760.
[24] Kalgutkar AP, Banerjee S. Interaction of ultrasonic guided waves with interfacial debonding in a stiffened composite plate under variable temperature and operational conditions. Ultrasonics 2024:107378.
[25] Doitrand A, Rubeck S, Meille S, Chevalier J, Steyer P, Gallois-Garreignot S. Influence of debonding and substrate plasticity on thin film multicracking. Theor Appl Fract Mech 2024;131:104375.
[26] Guo K, Sridhar N, Foo CC, Srinivasan BM. Energy release rate for steady-state fiber debonding in structural battery composites. Compos Sci Technol 2024;247:110416.
[27] Lauke B. Effect of particle size distribution on debonding energy and crack resistance of polymer composites. Comput Mater Sci 2013;77:53–60.
[28] Gilabert F, Van Tittelboom K, Tsangouri E, Van Hemelrijck D, De Belie N, Van Paepegem W. Determination of strength and debonding energy of a glass-concrete interface for encapsulation-based self-healing concrete. Cem Concr Compos 2017;79:76–93.
[29] Cao Y, Hu X, Ng CT, Smith ST. Diagnostic imaging of debonding in FRP-strengthened reinforced concrete structures using combinational harmonics generated by Rayleigh waves. Engng Struct 2024;314:118377.
[30] Bartley A, Chudalla N, Meschut G, Wibbeke TM. Low temperature debonding of toughened structural adhesive joints: a new approach to repairs in the automotive industry. Int J Adhes Adhes 2023;126:103486.
[31] Guo G, Hao C, Du B. Static and dynamic response characteristics of a ballastless track structure of a high-speed railway bridge with interlayer debonding under temperature loads. Engng Fail Anal 2023;151:107377.
[32] Yang Y, Cao J, Wu P, Luo T, Liang T, Yin H, et al. Effect of temperature on interface debonding behavior of graphene/graphene-oxide on cement-based composites. Surf Interfaces 2024;47:104198.
[33] Zhang W, Lin J, Huang Y, Lin B, Kang S. Temperature-dependent debonding behavior of adhesively bonded CFRP-UHPC interface. Compos Struct 2024;340:118200.
[34] Zhang X, Li W, Shao L-H, Li Y, Wang J. Micromechanics-based modeling of temperature-dependent effective moduli of fiber reinforced polymer composites with interfacial debonding. Compos A Appl Sci Manuf 2024;180:108049.
[35] Pirondi A, Giuliese G, Moroni F, Bernasconi A, Jamil A. In: Simulating the mixed-mode fatigue delamination/debonding in adhesively-bonded composite joints. Elsevier; 2015. p. 369–400.
[36] Kapuria S, Ahmed A. A coupled efficient layerwise finite element model for free vibration analysis of smart piezo-bonded laminated shells featuring delaminations and transducer debonding. Int J Mech Sci 2021;194:106195.
[37] Bruno D, Greco F. Delamination in composite plates: influence of shear deformability on interfacial debonding. Cem Concr Compos 2001;23(1):33–45.
[38] Allegri G, Zhang X. On the delamination and debond suppression in structural joints by Z-fibre pinning. Compos A Appl Sci Manuf 2007;38(4):1107–15.
[39] Bianchi F, Zhang X. A cohesive zone model for predicting delamination suppression in z-pinned laminates. Compos Sci Technol 2011;71(16):1898–907.
[40] Shen B, Wang K, Wang S, Li M, Dong L, Atluri SN. A fragile points method with a numerical-flux-based interface debonding model to simulate the delamination migration in composite laminates. Int J Solids Struct 2024;293:112758.
[41] Giuliese G, Pirondi A, Moroni F. A cohesive zone model for three-dimensional fatigue debonding/delamination. Procedia Mater Sci 2014;3:1473–8.
[42] Pan Z, Liu Q, Yan Z, Jiao Z, Bi L, Chan SH, et al. On the delamination of air electrodes of solid oxide electrolysis cells: a mini-review. Electrochem Commun 2022;137:107267.
[43] Nerat M, Juričić Đ. Modelling of anode delamination in solid oxide electrolysis cell and analysis of its effects on electrochemical performance. Int J Hydrogen Energy 2018;43(17):8179–89.
[44] Keane M, Mahapatra MK, Verma A, Singh P. LSM–YSZ interactions and anode delamination in solid oxide electrolysis cells. Int J Hydrogen Energy 2012;37(22):16776–85.
[45] Li N, Keane M, Mahapatra MK, Singh P. Mitigation of the delamination of LSM anode in solid oxide electrolysis cells using manganese-modified YSZ. Int J Hydrogen Energy 2013;38(15):6298–303.
[46] Khan MS, Xu X, Zhao J, Knibbe R, Zhu Z. A porous yttria-stabilized zirconia layer to eliminate the delamination of air electrode in solid oxide electrolysis cells. J Power Sources 2017;359:104–10.
[47] Fan Z, Pan F, Sun L, Wang D, Liu P. Multiscale investigation on bitumen-aggregate interfacial debonding using molecular dynamics and finite element method. Constr Build Mater 2023;397:132326.
[48] Jin X, Xue X. Computational fluid dynamics analysis of solid oxide electrolysis cells with delaminations. Int J Hydrogen Energy 2010;35(14):7321–8.
[49] Xia Z, Zhao D, Li Y, Deng Z, Kupecki J, Fu X, et al. Control-oriented dynamic process optimization of solid oxide electrolysis cell system with the gas characteristic regarding oxygen electrode delamination. Appl Energy 2023;332:120490.
[50] Xia Z, Zhao D, Zhou Y, Deng Z, Kupecki J, Fu X, et al. Control-oriented performance prediction of solid oxide electrolysis cell and durability improvement through retard oxygen electrode delamination with reverse operation. Energ Conver Manage 2023;277:116596.
[51] Paulino G, Zhang Z. Cohesive modeling of propagating cracks in homogeneous and functionally graded composites. 29; 2005.
[52] Yazdanparast R, Rafiee R. A rate-dependent cohesive zone model for dynamic crack growth in carbon nanotube reinforced polymers. Int J Solids Struct 2024:112932.
[53] Shen C, Xia X, Yi D, Xiao Z. A new cyclic cohesive zone model for fatigue damage analysis of welded vessel. Theor Appl Mech Lett 2024:100531.
[54] Zheng T, Chen N-Z. A cyclic cohesive zone model for predicting hydrogen assisted fatigue crack growth (FCG) of subsea pipeline steels. Int J Fatigue 2023;173:107707.
[55] Kumar A, Muthu N, Narayanan RG. Prediction of peel strength of sandwich sheets made of aluminium alloys fabricated by friction stir spot welding based hybrid process using cohesive zone modeling and finite element simulations. Engng Fail Anal 2024;162:108381.
[56] Shi C, Zhao Y, Zhu X, Wan X, Li B. Study on the shear failure mechanism of vulcanized rubber-metal bonding interface based on cohesive zone model. Int J Adhes Adhes 2024;134:103807.
[57] Shahriari M, Googarchin HS. Prediction of vehicle impact speed based on the post-cracking behavior of automotive PVB laminated glass: analytical modeling and numerical cohesive zone modeling. Engng Fract Mech 2020;240:107352.
[58] Shahriari M, Googarchin HS. Numerical investigation of the impact fracture performance of a composite laminated windshield considering the Park-Paulinho-Roesler cohesive zone model. Compos Struct 2020;249:112568.
[59] Hartlen DC, Montesano J, Cronin DS. Modelling of Mode I delamination using a stress intensity factor enhanced cohesive zone model. Compos Struct 2024;331:117928.
[60] Ashkpour A, Bidadi J, Googarchin HS. Measurement of the interfacial energy release rate (ERR) and cohesive law parameters of polyvinyl butyral laminated glass using a novel beam-type test specimen. Engng Fract Mech 2024;304:110170.
[61] Gheibi M, Shojaeefard M, Saeidi Googarchin H. Direct determination of a new mode-dependent cohesive zone model to simulate metal-to-metal adhesive joints. J Adhes 2019;95(10):943–70.

[62] Shi T, Zhang Y, Zhang X, Wang Y, Zheng K. A strength based thermo-mechanical coupled cohesive zone model for simulating heat flux induced interface debonding. Compos Sci Technol 2023;243:110255.
[63] Gheibi M, Shojaeefard MH, Googarchin HS, Zaeri A. A generalized-Park-Paulinho-Roesler cohesive zone model to simulate moderate ductile adhesive joints. Int J Adhes Adhes 2023;126:103489.
[64] Thiagarajan P, Sain T, Ghosh S. Bayesian calibration and uncertainty quantification of a rate-dependent cohesive zone model for polymer interfaces. Engng Fract Mech 2024;309:110374.
[65] Tian D, Gong Y, Zou L, Liu H, Zhang J, Zhao L, et al. Analytical solution for double cantilever beam based on cohesive zone model considering shear deformation. Engng Fract Mech 2024;312:110658.
[66] Zaeri AR, Saeidi Googarchin H. Analysis of automotive mixed-adhesive joints weakened by moist conditions: Experimental characterization and numerical simulation using cohesive zone model. Fatigue Fract Engng Mater Struct 2019;42(4):929–42.
[67] Motevalizadeh SM, Kavussi A, Mollenhauer K, Vuye C, Hasheminejad N. Use of a machine learning-based framework to approximate the input features of an intrinsic cohesive zone model of recycled asphalt mixes tested at low temperatures. Constr Build Mater 2023;373:130870.
[68] Du L, Wang Z, Gu T. A coupled thermo-mechanical cohesive zone model for strain rate-dependent fracture of hat-shaped specimens under impact. Engng Fract Mech 2023;289:109382.
[69] Kurushina V, Rajendran V, Prathuru A, Hossain M, Soman A, Horri B, Cai Q, et al. Thermomechanical deformation analysis of a tubular solid oxide steam electrolysis cell, In Proceedings of the 34th Thermal and fluid analysis workshop 2023 (TFAWS 2023), 21-25 August 2023, Maryland, USA. Washington: NASA, article number TFAWS23-ID-7. https://tfaws.nasa.gov/wp-content/uploads/TFAWS23-ID-7-Paper.pdf.
[70] ANSYS Inc. (n.d.-b). Fracture Analysis Guide. https://www.scribd.com/document/626512324/ANSYS-Mechanical-APDL-Fracture-Analysis-Guide.
[71] Hallett S, Harper P. Modelling delamination with cohesive interface elements. In Numerical modelling of failure in advanced composite materials. Elsevier; 2015. p. 55–72.
[72] ANSYS Inc. (n.d.-a). Cohesive Zone Material (CZM) Model. https://www.mm.bme.hu/~gyebro/files/ans_help_v182/ans_thry/thy_mat11.html.
[73] Kaptchouang NBN, Monerie Y, Perales F, Vincent P-G. Cohesive GTN model for ductile fracture simulation. Engng Fract Mech 2021;242:107437.
[74] Carreras L, Guillamet G, Quintanas-Corominas A, Renart J, Turon A. Mesoscale modelling of delamination using the cohesive zone model approach. In Multi-Scale Continuum Mechanics Modelling of Fibre-Reinforced Polymer Composites. Elsevier; 2021. p. 555–77.
[75] Sadeghi-Fadaki S, Zangeneh-Madar K, Valefi Z. The adhesion strength and indentation toughness of plasma-sprayed yttria stabilized zirconia coatings. Surf Coat Technol 2010;204(14):2136–41.
[76] Mantry S, Mishra BK, Chakraborty M. Parametric appraisal of process parameters for adhesion of plasma sprayed nanostructured YSZ coatings using taguchi experimental design. Scientific World J 2013;2013(1):527491.
[77] Ghasemi R, Vakilifard H. Plasma-sprayed nanostructured YSZ thermal barrier coatings: thermal insulation capability and adhesion strength. Ceram Int 2017;43(12):8556–63.
[78] Prathuru, A. Structural and residual strength analysis of metal-to-metal adhesively bonded joints; 2019.
[79] Britannica. Silver. In Britannica; 2024. https://www.britannica.com/science/silver.
[80] SubsTech. (n.d.). Fine silver (Substech). https://www.substech.com/dokuwiki/doku.php?id=fine_silver.
[81] The Engineering ToolBox. (n.d.). Linear expansion coefficients. In The Engineering ToolBox. https://www.engineeringtoolbox.com/linear-expansion-coefficients-d_95.html.
[82] Wikipedia. (n.d.-e). Silver. In Wikipedia. https://en.wikipedia.org/wiki/Silver.
[83] Wikipedia. (n.d.-d). Nickel (II) Oxide. https://en.wikipedia.org/wiki/Nickel(II)_oxide.
[84] Wikipedia. (n.d.-b). Gadolinium-doped ceria. https://en.wikipedia.org/wiki/Gadolinium-doped_ceria.
[85] Cerpotech. (n.d.-a). Ceria, gadolinium-doped, CGO82. https://www.cerpotech.com/products/ceria-gadolinium-CGO82.
[86] Badwal S, Fini D, Ciacchi F, Munnings C, Kimpton J, Drennan J. Structural and microstructural stability of ceria–gadolinia electrolyte exposed to reducing environments of high temperature fuel cells. J Mater Chem A 2013;1(36):10768–82.
[87] Bowen MS, Johnson M, McQuade R, Wright B, Kwong K-S, Hsieh PY, et al. Electrical properties of gadolinia-doped ceria for electrodes for magnetohydrodynamic energy systems. SN Appl Sci 2020;2:1–9.
[88] Jia D, Zhou A, Ling Y, An K, Stoica A, Wang X. Effect of porosity on the mechanical properties of YSZ/NiO composite anode materials. World J Eng 2010;7(3):489.
[89] Kushi T, Sato K, Unemoto A, Hashimoto S, Amezawa K, Kawada T. Elastic modulus and internal friction of SOFC electrolytes at high temperatures under controlled atmospheres. J Power Sources 2011;196(19):7989–93.
[90] Amezawa K, Kushi T, Sato K, Unemoto A, Hashimoto S, Kawada T. Elastic moduli of Ce0. 9Gd0. 1O2− δ at high temperatures under controlled atmospheres. Solid State Ion 2011;198(1):32–8.
[91] Yamada A., N. S. (2019). Preparation and Thermoelectric Properties of Nickel Oxide added Strontium Ferrite Nano-Composite. HSOA Journal of Modern Chemical Sciences. https://www.heraldopenaccess.us/openaccess/preparation-and-thermoelectric-properties-of-nickel-oxide-added-strontium-ferrite-nano-composite#:~:text=Electrical%20properties%20and%20thermal%20conductivity,97.3%CE%BCWm%2D1K%2D2.
[92] Hayashi H, Kanoh M, Quan CJ, Inaba H, Wang S, Dokiya M, et al. Thermal expansion of Gd-doped ceria and reduced ceria. Solid State Ion 2000;132(3–4):227–33.
[93] Alghazzawi TF, Lemons J, Liu P, Essig ME, Bartolucci AA, Janowski GM. Influence of low-temperature environmental exposure on the mechanical properties and structural stability of dental zirconia. J Prosthodontics: Implant Esthetic Reconstruct Dentistry 2012;21(5):363–9.
[94] Ceramic Industry. (n.d.). Ceramic Materials Properties Charts (Ceramic Industry). https://www.ceramicindustry.com/ceramic-materials-properties-charts/.
[95] MakeItFrom. Yttria Partially Stabilized Zirconia (TZP); 2020. https://www.makeitfrom.com/material-properties/Yttria-Partially-Stabilized-Zirconia-TZP.
[96] AZOnano. Yttria Stabilized Zirconia, YSZ (ZrO2 / Y2O3) Nanoparticles. AZOnano; 2013. https://www.azonano.com/article.aspx?ArticleID=3374.
[97] Wikipedia. (n.d.-f). Ultimate Tensile Strength. https://en.wikipedia.org/wiki/Ultimate_tensile_strength.
[98] Kondoh J, Shiota H, Kawachi K, Nakatani T. Yttria concentration dependence of tensile strength in yttria-stabilized zirconia. J Alloy Compd 2004;365(1–2):253–8.
[99] Radovic M, Lara-Curzio E, Trejo RM, Wang H, Porter W. Thermophysical Properties of YSZ and Ni-YSZ as a Function of Temperature and Porosity. Advances in Solid Oxide Fuel Cells II: Ceramic Engineering and Science Proceedings 2006;27:79–85.
[100] Cerpotech. (n.d.-b). Lanthanum strontium cobalt ferrite, LSCF (Cerpotech). https://www.cerpotech.com/products/lanthanum-stontium-cobalt-ferrite-LSCF.
[101] Huang B, Malzbender J, Steinbrech R, Wessel E, Penkalla H, Singheiser L. Mechanical aspects of ferro-elastic behavior and phase composition of La0. 58Sr0. 4Co0. 2Fe0. 8O3− δ. J Membrane Sci 2010;349(1–2):183–88.
[102] Matmatch. (n.d.). Lanthanum strontium cobalt ferrite (LSCF) Powder. https://matmatch.com/materials/cerpo016-lanthanum-strontium-cobalt-ferrite-lscf-powder.
[103] Wikipedia. (n.d.-c). Lanthanum. https://en.wikipedia.org/wiki/Lanthanum.
[104] Britannica. (n.d.). Lanthanum. https://www.britannica.com/science/lanthanum.
[105] Wikipedia. (n.d.-a). Cobalt. https://en.wikipedia.org/wiki/Cobalt.
[106] Jiang SP. Development of lanthanum strontium cobalt ferrite perovskite electrodes of solid oxide fuel cells – a review. Int J Hydrogen Energy 2019;44(14):7448–93.